



Research Article

Synthesis, formation mechanism, and intrinsic physical properties of several As/P-containing MAX phases



Hongxiang Chen^{a,c,d,1,*}, Sheng Li^{a,1}, Jun Deng^{b,1}, Zhilong Zhang^a, Jianeng Huang^{a,c},
Fa Chang^{a,c}, Li Huang^a, Shixuan Du^{b,e,f,*}, Pinqiang Dai^{a,c,*}

^a School of Materials Science and Engineering, Fujian University of Technology, Fuzhou 350118, China

^b Institute of Physics & University of Chinese Academy of Sciences, Chinese Academy of Sciences, Beijing 100190, China

^c Fujian Provincial Key Laboratory of Advanced Materials Processing and Application, Fuzhou 350118, China

^d Center for Advanced Energy and Functional Materials, Fujian University of Technology, Fuzhou 350118, China

^e Songshan Lake Materials Laboratory, Dongguan 523808, China

^f CAS Key Laboratory of Vacuum Physics, Beijing 100049, China

ARTICLE INFO

Article history:

Received 10 April 2022

Revised 10 June 2022

Accepted 13 June 2022

Available online 9 July 2022

Keywords:

MAX phase

Molten-salt synthesis

Chemical reaction route

Metallic ceramics

Formation mechanism

Quasi-harmonic approximation

ABSTRACT

321 phases are an atypical series of MAX phases, in which A = As/P, with superior elastic properties, featuring in the MA-triangular-prism bilayers in the crystal structure. Until now, besides Nb₃As₂C, the pure phases of the other 321 compounds have not been realized, hampering the study of their intrinsic properties. Here, molten-salt sintering (MSS) and solid-state synthesis (SSS) were applied to synthesize As/P-containing 321 phases and 211 phases. Analyzing the phase composition of the end-product via multiple-phase Rietveld refinement, we found that MSS can effectively improve the purity of P-containing MAX phases, with the phase content up to 99% in Nb₃P₂C and 75.4(5)% in Nb₂PC. In contrast, MSS performed poorly on As-containing MAX phases, only 8.9(4)% for Nb₃As₂C and 64(2)% for Nb₂AsC, as opposed to the pure phases obtained by SSS. The experimental analyses combined with first-principles calculations reveal that the dominant formation route of Nb₃P₂C is through NbP + Nb + C → Nb₃P₂C. Moreover, we found that the benefits of MSS on P-containing MAX phases are on the facilitation of three considered chemical reaction routes, especially on Nb₂PC + NbP → Nb₃P₂C. Furthermore, the intrinsic physical properties and Fermi surface topology of two 321 phases consisting of electron, hole, and open orbits are revealed theoretically and experimentally, in which the electron carriers are dominant in electrical transport. The feasible synthesis methods and the formation mechanism are instructive to obtain high-purity As/P-containing MAX phases and explore new MAX phases. Meanwhile, the intrinsic physical properties will give great support for future applications on 321 phases.

© 2022 Published by Elsevier Ltd on behalf of The editorial office of Journal of Materials Science & Technology.

1. Introduction

MAX phases are a series of metallic ceramics with a general chemical formula [1], M_{n+1}AX_n, in which the crystal structure can be viewed as an alternating stack of one MA-triangular-prism layer and *n* MX-octahedron layers [2], *n* = 1–3. In the formula, M means the transition metals, A is the main group elements, and X is C/N. The excellent combination of thermal, electrical, and mechanical performances makes MAX phases show promising potential on the structural and conductive components at high temperatures [1,3,4].

Besides, as the source materials to synthesize two-dimensional transition metal carbides (MXene) [5–8], lots of attention is focused on these series of materials.

In recent years, the family of MAX phases has been growing fast; more than 80 kinds of MAX phases have been experimentally discovered [7,9–14]. In 2019, an atypical series of As/P-containing MAX phases named 321 phases deviating the general chemical formula, including Nb₃As₂C, Nb₃P₂C, Ta₃P₂C, and V₃As₂C, was added to the MAX family [2], feathering in the MA-triangular-prism bilayer in contrast to the single-layered one in other MAX phases. Nb₃As₂C was found to possess a high bulk modulus up to 225(3) GPa [2], and excellent elastic properties were predicted [2,15]. Among four 321 phases, due to the relatively low toxicity, low density, and superior elastic performance, Nb₃P₂C was predicted to possess the best application prospect among all 321 phases. Until

* Corresponding authors.

E-mail addresses: hungxchen@163.com (H. Chen), sxdu@iphy.ac.cn (S. Du), pqdai@126.com (P. Dai).

¹ These authors contributed equally to this work.

now, only Nb₃As₂C has been synthesized in the pure phase. Using the solid-state synthesis (SSS) method, the phase content of the end product cannot be higher than 60%. And the underlying reason why the pure phase is hard to be obtained is still unclear. Meanwhile, As/P-containing 211 phases also show outstanding mechanical and thermal properties among MAX phases [16–18]. However, due to the lack of the high-purity Nb₂PC sample, most works are focused on Nb₂AsC [16,18–20]. The pure-phase synthesis of As/P-containing MAX phases has been the Achilles to the experimental study of their intrinsic properties and exploration of their further applications. Therefore, a new synthesis method is urgently needed to obtain pure As/P-containing MAX phases.

Inspired by these, we attempt to study the pure-phase synthesis, formation mechanism, and intrinsic physical properties of As/P-containing MAX phases. Molten-salt synthesis (MSS) has been widely used in crystal growth and chemical synthesis and proved to be applicable to the synthesis of MAX phases [14,21–29] which is helpful to improve the purity and reduce the sintering temperature (T_s). In this work, we adopted an MSS method to synthesize As/P-containing MAX phases, including Nb₃P₂C, Nb₃As₂C, Nb₂PC, and Nb₂AsC. Meanwhile, a comparison with the phase content of the ones prepared by the SSS method was made. The effect of T_s on the phase content of the end-product was systematically analyzed. As a result, we suggest that MSS and SSS are suitable to synthesize P-containing MAX phases and As-containing MAX phases, respectively. Meanwhile, the optimized sintering process of each phase was given here. Revealing the synthesis mechanism of Nb₃P₂C, our first-principles calculations show that the reaction route of $2\text{NbP} + \text{Nb} + \text{C} \rightarrow \text{Nb}_3\text{P}_2\text{C}$ has the lowest Gibbs energy than others, which is consistent with the experimental results. Meanwhile, the mechanism of the enhancement of phase content by MSS was revealed. Using the pure samples of Nb₃As₂C and Nb₃P₂C, with the help of DFT results, the intrinsic properties were systematically studied, including the electronic structures, magneto-transport, thermo-electric properties, and magnetism. Our work provides applicable routes to synthesize As/P-containing MAX phases, and the intrinsic physical properties herein are essential for future applications.

2. Experimental methods

Molten-salt synthesis method: A two-step sintering method was used to synthesize As/P-containing MAX phases. At first, high purity M = Nb (99.9%, 200 mesh, Alfa), As (99.9%, 200 mesh, Aladdin) or P (red phosphorus, 99%, 100 mesh, Aladdin), and graphite (99.95%, 325 mesh, Aladdin) powders in a total amount of 1 g were mixed in a molar ratio of 3 : 2 : 1.05 and pelletized and then were sealed in a silica tube (inner diameter: 19 mm, outer diameter: 25 mm, length: 8 cm) under a high vacuum. To avoid explosion and the formation of white phosphorous which is highly toxic, the tubes were slowly heated to 650 °C in 12 h and kept sintering for more than 36 h. If the sample was not pelletized or the heating duration at 650 °C was not long enough, the tube will explode. Then heat the tube to 850 °C in 2 h, kept sintering for 12 h, and then furnace-cooled to room temperature. The outcome after the first-step sintering is NbP + Nb + C. Secondly, the outcome from the first step was mixed with the salts KCl / NaCl (1 : 3) in a molar ratio of 1 : 10. Loaded the mixture into a crucible and sealed the silica tube under a high vacuum. The alumina crucible was wrapped in graphite paper. The silica tubes were heated to the T_s in 4 h and kept sintering for 15 h. Removing the salts by water washing, the end-product was obtained.

Solid-state synthesis method: A two-step SSS method was applied [2], using the elemental powders of M, A, and X elements as starting materials. The first step is the same as the one in MSS. Secondly, the pre-sintered samples were crushed, pelletized, and

the pre-sintered sample was re-sealed in silica tubes. The samples were heated to T_s and kept sintering for more than 10 h, and then furnace-cooled to room temperature.

Phase composition analysis: Powder X-ray diffraction (PXRD) was performed at room temperature using a D8 Advance diffractometer (Bruker, Germany) with a graphite monochromator with Cu-K α radiation in a reflection mode. First, after analyzing the XRD pattern of end-products, the phase composition was qualifiedly identified based on the PDF2-2010 database and the reported crystal structure information of 321 phase [2]. Then, multi-phase Rietveld refinement [31–33] was applied to determine the phase content of each as-identified phase by using the FULLPROF program suite [30]. The reliability factors of refinement results, including the weighted profile R-factor (R_{wp}), profile R-factor (R_p), and goodness of fit (GoF), were given. It should be noted that the phase content means the mole ratio of each phase in the end-product.

The microstructure and chemical composition were obtained through filed mission scanning electron microscopy (FESEM) (NovaNano EM450, FEI, USA) equipped with an energy-dispersive spectrometer (EDS) (Model Link-Isis, Oxford, England).

Selected area electron diffraction (SAED) and high-resolution transmission electron microscopy (HRTEM) images of Nb₃P₂C were collected using a JEOL JEM-2100 transmission electron microscope operated at 200 KeV equipped with an energy dispersion X-ray spectroscopy (EDS) component.

DFT calculations: The density functional theory (DFT) calculations were carried out by the Vienna *Ab initio* Simulation Package (VASP) [34,35] with the projector augmented wave (PAW) [36] pseudopotentials and the Perdew, Burke, and Ernzerhof (PBE) [37] for the exchange-correlation functional. The cutoff energy for the plane wave expansion was 500 eV, and the Brillouin zones were sampled by a Monkhorst-Pack [38] k -point mesh $0.02 \times 2\pi \text{ \AA}^{-1}$ in the self-consistent calculation. A denser k -mesh $0.01 \times 2\pi \text{ \AA}^{-1}$ and $0.008 \times 2\pi \text{ \AA}^{-1}$ were applied for density of states and Fermi surface, respectively. Atomic positions and lattice parameters were relaxed until all the forces were less than $10^{-3} \text{ eV \AA}^{-1}$. The Gibbs free energy of the possible reaction routes was calculated by using the quasi-harmonic approximation (QHA) implemented in the PHONOPY code [39], which concludes a part of the anharmonic effect. The Gibbs energy (G) is defined as

$$G(T, p) = \min[U(V) + F_{\text{phonon}}(T, V) + pV]$$

where T is the absolute temperature, U is the internal lattice energy, V is lattice volume, p is the pressure, and F_{phonon} is the phonon (Helmholtz) free energy:

$$F_{\text{phonon}} = \varphi + \frac{1}{2} \sum_{\mathbf{q}, \nu} \hbar\omega(\mathbf{q}, \nu) + k_B T \sum_{\mathbf{q}, \nu} \ln[1 - \exp(-\hbar\omega(\mathbf{q}, \nu)/k_B T)]$$

where ω is the phonon frequency at \mathbf{q} point and mode ν , \hbar Planck's constant, k_B Boltzmann's constant, φ the ground state energy.

Physical Property Characterizations: High-pressure sintering was used to obtain the compacted bulk sample. Before sintering, the sample was pressed into a pellet (Φ 6 mm \times 3 mm). The pre-pressed pellet was sealed in a gold capsule and put into a graphite tube furnace thereafter. High-pressure experiments were performed in a DS6 \times 600 T cubic-anvil-type high-pressure apparatus. After sintering at 1000 °C with a pressure of 5 GPa for a half-hour, the bulk sample was obtained. The phase composition of the pelletized sample was characterized by XRD, and the pure phase remained. Then the sample was cut and polished into a thin plate (4 mm \times 1 mm \times 200 μm). The magneto-transport, including the field dependences of Hall resistance (Fig. S11 in the Supplementary Material) and magnetoresistance (MR) (Fig. S13) of Nb₃As₂C, was measured on a PPMS-9T (Quantum Design) equipped with a dilution refrigerator insert, using a six-probes measurement method.

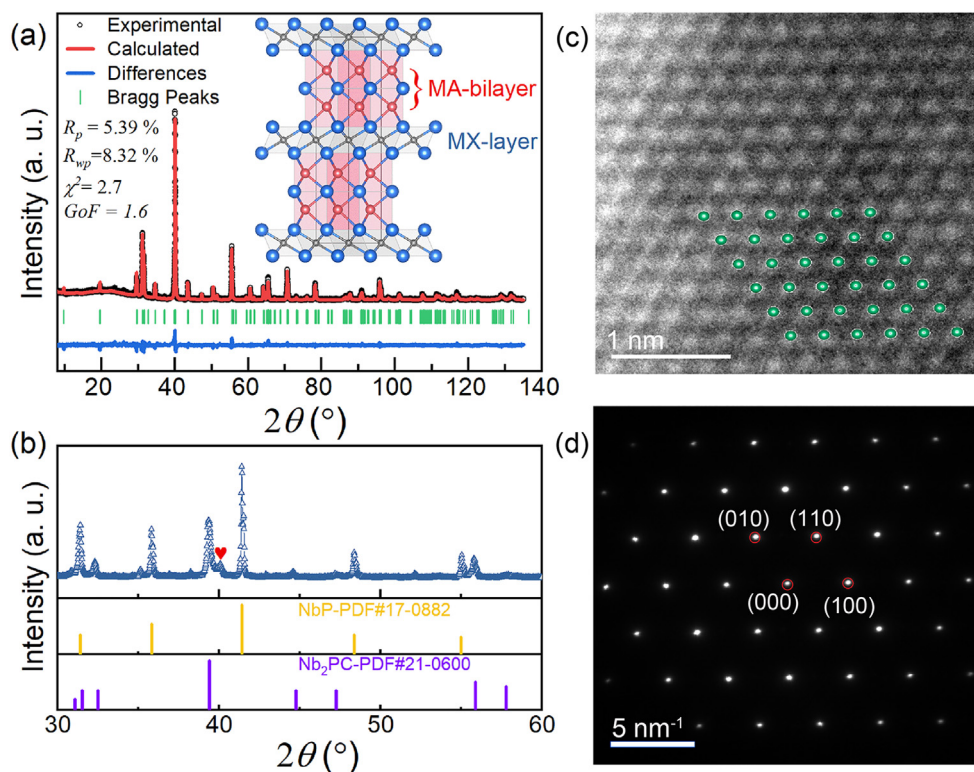


Fig. 1. Phase-composition and crystal-structure characterizations of $\text{Nb}_3\text{P}_2\text{C}$ prepared by MSS. (a) XRD pattern and Rietveld refinement results of as-prepared $\text{Nb}_3\text{P}_2\text{C}$ sintered at 1200 °C. The inset is the crystal structure of 321 phases viewed from the [110] direction. (b) XRD pattern of the sample sintered at 1150 °C. The ICDD PDF cards of NbP (PDF#17-0882) and Nb_2PC (PDF#21-0600) are given below the XRD pattern. The red-heart symbol indicates the characteristic Bragg peak (105) of $\text{Nb}_3\text{P}_2\text{C}$. (c) HRTEM image of $\text{Nb}_3\text{P}_2\text{C}$, the green atoms can be regarded as a single layer of Nb/P atoms. (d) SAED pattern of $\text{Nb}_3\text{P}_2\text{C}$ collected along the $\langle 001 \rangle$ zone axis.

The bulk sample prepared by high-pressure sintering is not large enough for thermoelectric measurements. Therefore, sparking-plasma sintered pellets ($\Phi 15 \times 3$ mm) sintered at 1200 °C for a half-hour with a pressure of 40 MPa using an SPS (SPS-5T-5-III, Chenhua, Shanghai) were used to characterize the thermoelectrical properties. The phase composition was re-checked by XRD, and the pure phase remained. Then the sample was cut and polished to the size of 3 mm \times 3 mm \times 10 cm. A thermoelectric properties measurement system (CTA-3s, Beijing Cryoall Science and Technology Co.) system was used to simultaneously determine the electrical conductivity (σ) and Seebeck coefficient (S) under a low-pressure helium atmosphere from 300 K to 700 K.

The thermal conductivity is obtained from $\kappa = D C_p d$, where the thermal diffusivity coefficient (D) was measured with Linseis LFA-1000 from room temperature to 873 K, the density (d) was determined by using the Archimedes drainage method, and the DFT-calculated results (Fig. S14) of specific heat (C_p) was used.

The magnetic properties of $\text{Nb}_3\text{As}_2\text{C}$ and $\text{Nb}_3\text{P}_2\text{C}$ were measured on a SQUID-7 T (Quantum Design) in the temperature range of 2–300 K, with the loaded sample mass around 15 mg.

3. Results and discussion

3.1. Synthesis of $\text{Nb}_3\text{P}_2\text{C}$

A comparison of the end-products using different T_s was studied, including 1100, 1150, 1200, and 1250 °C. When $T_s = 1100$ °C, no 321 phase was formed. When T_s is increased to 1150 °C, the (105) peak of $\text{Nb}_3\text{P}_2\text{C}$ can be observed, as indicated by the red-heart symbol in Fig. 1(b), along with the main phases of Nb_2PC and NbP. When T_s is increased to 1200 °C, an almost pure phase ($> 99\%$) of $\text{Nb}_3\text{P}_2\text{C}$ can be obtained, as shown in Fig. 1(a). Compared

with the phase content of samples prepared by the SSS method ($< 60\%$), the purity is significantly promoted. The lattice parameters are $a = b = 3.30735(6)$ Å and $c = 18.0668(4)$ Å in a space group $P6_3/mmc$ (No. 194) with the refinement parameters $R_p = 5.39\%$, $R_{wp} = 8.32\%$, $\chi^2 = 2.7$, and $\text{GoF} = 1.6$. The information about the atomic positions and Bragg diffraction peaks are listed in Tables S1 and S2 in the Supplementary Material, respectively. The lattice parameters are close to the reported values using multi-phases refinement [2].

The crystal structure of the as-prepared $\text{Nb}_3\text{P}_2\text{C}$ was checked by the HRTEM and SAED results [40]. The HRTEM image (Figs. 1(c) and S1) shows the hexagonal arrangement in the (001) plane. As shown in Fig. 1(d), the SAED pattern can be well indexed by the diffraction pattern of the as-determined crystal structure collected along the $\langle 001 \rangle$ zone axis. The as-determined d -spacing of (100) is 2.868 Å, close to the Rietveld refinement results of 2.864 Å.

Further increasing the temperature to 1250 °C, the results are similar. On the other hand, due to the limited operating temperature of quartz tubes and the etching effects of molten salts at high temperatures, T_s is not supposed to be higher than 1300 °C. Therefore, we propose that the proper T_s to synthesize $\text{Nb}_3\text{P}_2\text{C}$ by the MSS method is in the range of 1200–1300 °C.

The micro-morphology and chemical composition of the MSS-prepared $\text{Nb}_3\text{P}_2\text{C}$ was characterized. As shown in Fig. 2(a, b), the particle size of the MSS-prepared sample is in the range of 1–30 μm , with typical hexagonal morphology. As shown in Fig. 2(b), the layered and hexagonal single particle with a grain size of ~ 25 μm reveals the hexagonal and layered crystal characteristics of MAX phases. As determined by the EDS (Fig. 2(c)), the chemical ratio of Nb : P equal to 60.5 : 39.5 is close to the nominal composition. And the EDS mapping analysis demonstrates that they are homogeneously distributed, as shown in Fig. 2(d, e). In contrast,

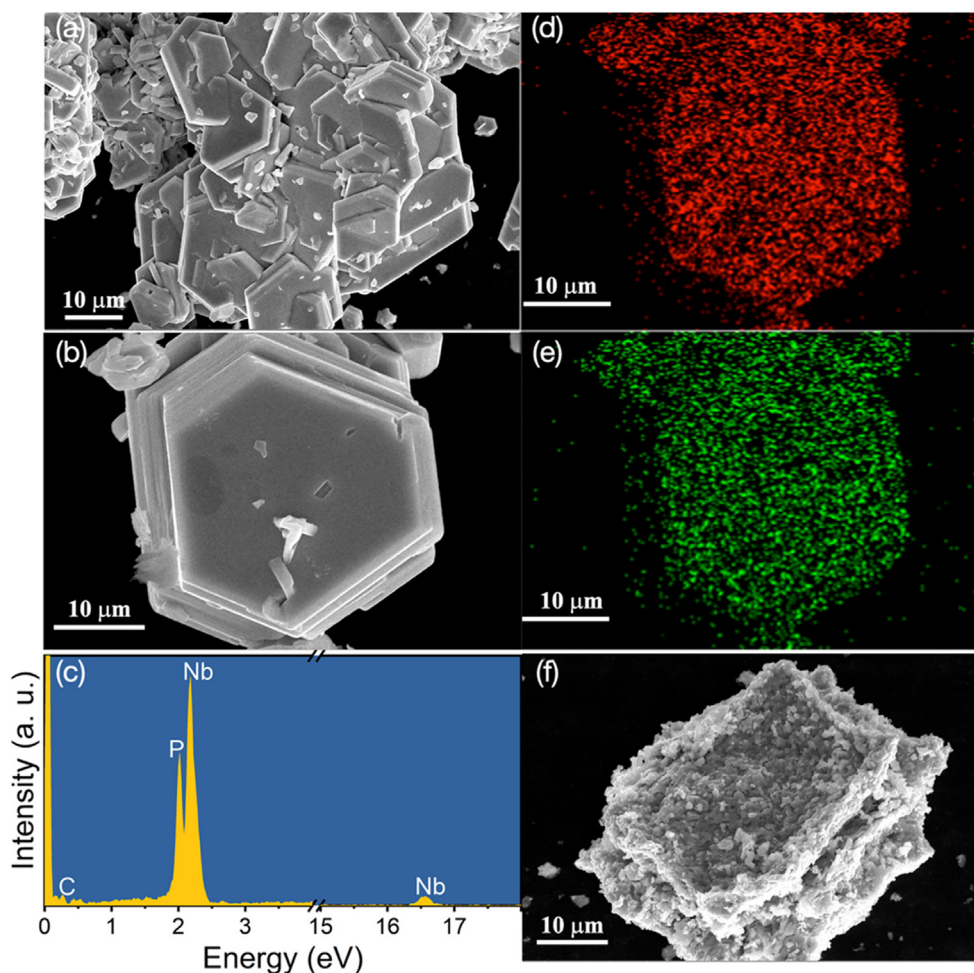
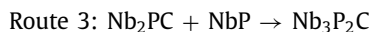


Fig. 2. SEM and EDS mapping results of $\text{Nb}_3\text{P}_2\text{C}$. (a, b) Micro-morphology of as-prepared $\text{Nb}_3\text{P}_2\text{C}$ powder by MSS. (c) EDS result of the particle in (b). EDS mapping analysis of (d) Nb and (e) P. (f) Morphology of the one prepared by SSS.

the grain size of the SSS-prepared sample is much smaller, around $1\ \mu\text{m}$; and the particles are clustered together (Fig. 2(f)), in which the boundary and the morphology of the particles are obscure. See more SEM images in Fig. S2.

3.2. Formation mechanism of $\text{Nb}_3\text{P}_2\text{C}$

To reveal the mechanism of the phase formation of $\text{Nb}_3\text{P}_2\text{C}$, three chemical reaction routes as follows were considered, and different starting materials on the left side of each reaction route use a one-step sintering process with $T_s = 1200\ \text{°C}$.



The XRD patterns and refinement results of the end-product using different reaction routes of SSS and MSS are shown in Fig. 3(a, b), respectively. In the SSS scheme, the best results are given by Route 1, using NbP, Nb, and C as the starting materials, in which the phase content of $\text{Nb}_3\text{P}_2\text{C}$ is up to 57.5(6)%, along with the by-product of NbP (16.2(3)%), Nb_2PC (8.9(4)%), NbC (4.1(1)%), and C (13.3(4)%). In contrast to the relatively high phase content in Route 1, the phase content of 321 phases of Route 2 and Route 3 are 24.6(6)% and 15.5(3)%, respectively. More details about the Rietveld

refinement results are given in Figs. S3 and S4 and Tables S3 and S4. Noted that the starting material Nb_2PC in Route 3 was prepared by the MSS method (75.5%).

Surprisingly, in the MSS scheme, the phase content is enhanced significantly in all three reaction routes as shown in Fig. 3(c), in which the comparison of phase content between MSS and SSS is given. The details of the phase composition of samples in Fig. 3(a, b) are summarized in Tables S3 and S4. Similar to the SSS scheme, Route 1 is superior to the others, the phase content is up to 98%. In Route 2, the phase content is increased to 58(1)%, along with the by-product of Nb_2PC (30.4(8)%) and NbP (11.3(5)%). Among the three routes, Route 3 shows the most significant enhancement in phase content up to 88.7(7)%, with a slight impurity of NbP. It is supposed to obtain the pure phase by adjusting the chemical ratio via this reaction route.

To reveal the underlying mechanism behind reactions, we resort to first-principles calculations. The thermal dynamics of each reaction route were theoretically calculated. The results demonstrate that the Gibbs energy change (ΔG) of all reaction routes is negative, suggesting that all routes are thermal-dynamically favorable. As shown in Fig. 3(d), in the calculated temperature range, Route 1 has a lower ΔG than the others. Therefore, Route 1 will take the privilege thermal-dynamically. Furthermore, the theoretical results match well with the results of SSS (Fig. 3(a)), in which Route 3 is the hardest. Meanwhile, no obvious decline in T was found in the MSS scheme in a comparison with the SSS scheme. Based on the as-calculated ΔG and the comparison between the yield of the tar-

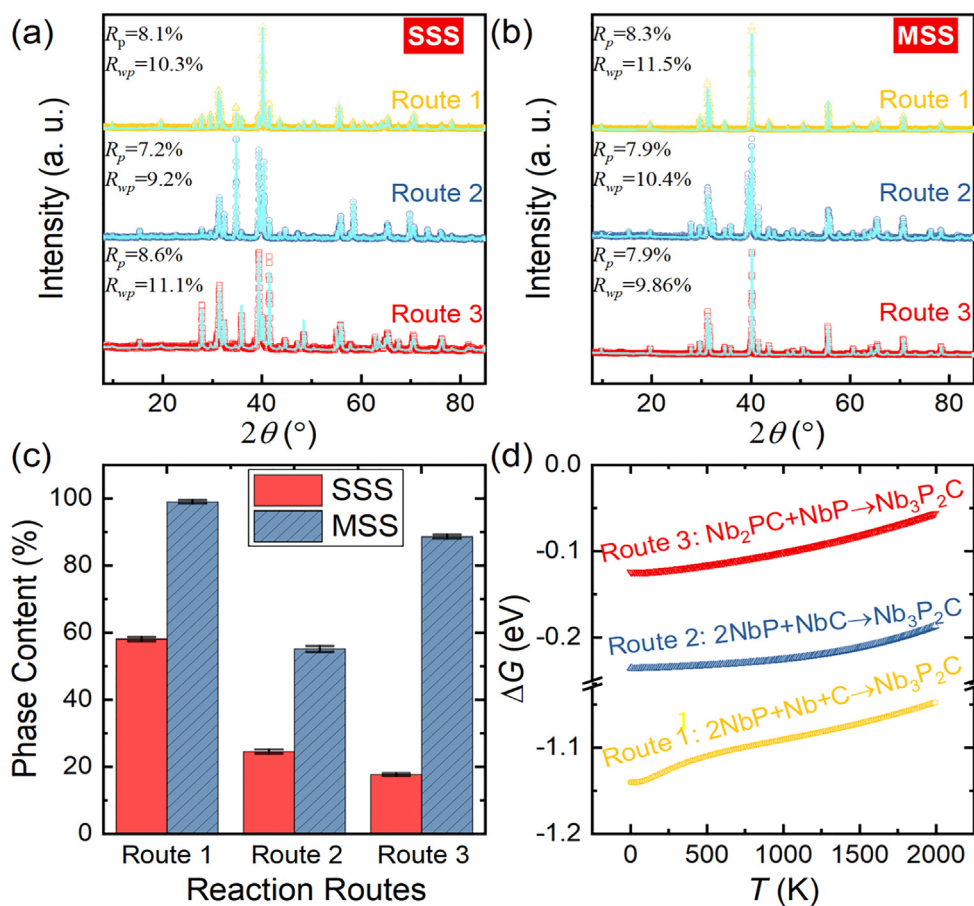


Fig. 3. Chemical reaction routes of $\text{Nb}_3\text{P}_2\text{C}$. XRD patterns of samples prepared via different chemical reaction routes by (a) SSS and (b) MSS. The cyan curves are the Rietveld refinement results. (c) Phase content of 321 phases prepared by SSS and MSS. (d) Calculated Gibbs free energy change of different chemical reaction routes to synthesize $\text{Nb}_3\text{P}_2\text{C}$ and $\text{Nb}_3\text{As}_2\text{C}$.

get phase using SSS/MSS via each route, we suggest that MSS performed so well on $\text{Nb}_3\text{P}_2\text{C}$ because the molten salt will facilitate the diffusivity of the reactants and the reactivity of the thermodynamically less-favored reaction routes, especially on the reaction route of $\text{Nb}_2\text{PC} + \text{NbP} \rightarrow \text{Nb}_3\text{P}_2\text{C}$.

3.3. MSS vs SSS of As/P-containing MAX phases

Now, we have obtained the pure phase of $\text{Nb}_3\text{As}_2\text{C}$ [2] and $\text{Nb}_3\text{P}_2\text{C}$ by SSS and MSS, respectively. Furthermore, we wonder whether the MSS is valuable to synthesize other As/P-containing MAX phases, including Nb_2PC , Nb_2AsC , and $\text{Nb}_3\text{As}_2\text{C}$. Therefore, we applied both SSS and MSS to them with different T_s in the range of 1000–1250 °C. To demonstrate the feasibility of each method to prepare corresponding phases, the phase content of target products prepared by SSS and MSS with optimal sintering process are summarized in Fig. 4(a).

The XRD patterns of “ Nb_2PC ” prepared by SSS using different T_s are given in Fig. S5. When T_s is lower than 1050 °C, no Nb_2PC was detected in the end-product which was composed of Nb, C, and NbP. The phase content of Nb_2PC can reach 41.90(1)% when T_s is ~ 1150 °C with byproducts of NbP (21.40(6)%), NbC (8.43(3)%), C (26.10(13)%), and Nb (2.15(12)%). It should be noted that obvious impurities of unreacted Nb and C are found in the samples prepared by SSS. However, further increasing T_s will decrease the purity of the target material and take more impurity of $\text{Nb}_3\text{P}_2\text{C}$ in the end-product.

The XRD patterns of Nb_2PC prepared by MSS are shown in Fig. S6. Similar to the SSS case, the Nb_2PC formed when $T_s = 1050$ °C.

The phase content of samples prepared by MSS is much higher, and the unreacted graphite was much reduced. When $T_s = 1150$ °C, the phase content of Nb_2PC reaches up to 75.4(5)%, with the by-products of $\text{Nb}_3\text{P}_2\text{C}$ (19.1(3)%) and NbP (5.5(2)%). Meanwhile, the accurate lattice parameters of Nb_2PC are obtained by Rietveld refinement, $a = b = 3.28969(12)$ Å and $c = 11.55066(58)$ Å, which are close to the reported values ($a = 3.286$ Å, $c = 11.56$ Å) [41]. The refined atomic positions and diffraction peaks of Nb_2PC are listed in Tables S5 and S6, respectively.

As shown in Fig. 4(b), by further increasing the T_s , the phase content of $\text{Nb}_3\text{P}_2\text{C}$ increases obviously, while the content of Nb_2PC decreases, see the detailed data in Fig. S6 and Table S7. When $T_s = 1250$ °C, the main phases are Nb_2PC (47(1)%) and $\text{Nb}_3\text{P}_2\text{C}$ (30(1)%). At high temperatures, various chemical reactions take place. The subtle competition between the phase formation of $\text{Nb}_3\text{P}_2\text{C}$ and Nb_2PC is the key to obtaining high-purity samples. When T_s is around 1100–1150 °C, it is preferred to form Nb_2PC but not $\text{Nb}_3\text{P}_2\text{C} + \text{NbP}$. And we suggest that the purity can be further improved by minor adjustments to the sintering process and the elemental ratio.

The pure phase of $\text{Nb}_3\text{As}_2\text{C}$ has been reported in our previous work [2] with a T_s of ~ 1280 °C. Here, we find that almost pure Nb_2AsC can be obtained by SSS using a $T_s = 1100$ °C, as shown in Figs. S7 and S8. When $T_s > 1100$ °C, by-products of NbAs and NbC appeared. According to the refinement results, the lattice parameters of Nb_2AsC are $a = b = 3.32093(9)$ Å and $c = 11.92148(35)$ Å, which are close to the reported value [18,41]. The obtained atomic positions and diffraction peaks are given in Tables S8 and S9. However, we find that the MSS method is not applicable to synthesizing

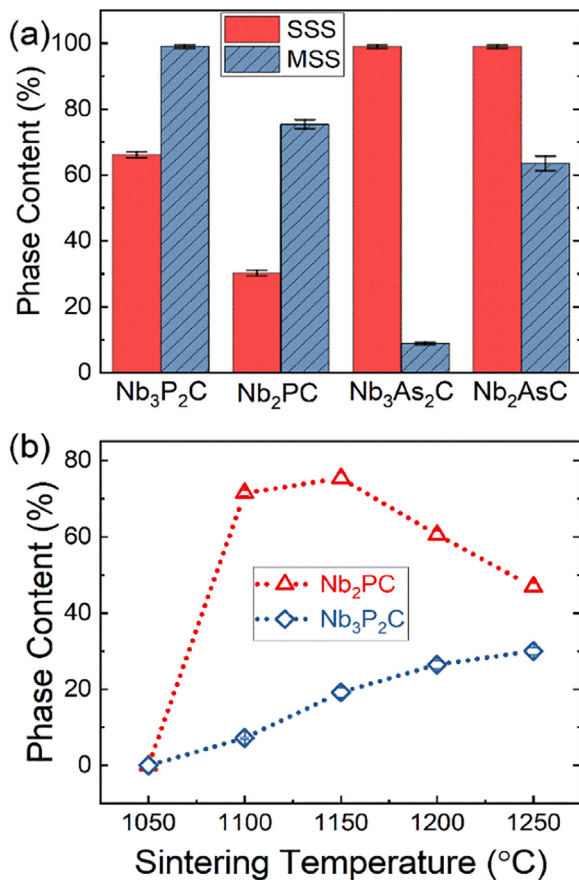


Fig. 4. Phase content of As/P-containing MAX phases. (a) Phase content of target products prepared by SSS and MSS with optimal sintering process. (b) Phase content of Nb₂PC and Nb₃P₂C in the end-product of “Nb₂PC” using different T_s by MSS.

As-containing MAX phases. For Nb₃As₂C, as shown in Fig. S9, the phase formation of Nb₃As₂C occurs when $T_s = 1050$ °C. However, the phase content will not be improved obviously by increasing the T_s . The main phases are Nb₂AsC and NbAs with only 8.9(4)% Nb₃As₂C. In the MSS case of Nb₂AsC, the phase content is reduced to 64(2)% with a $T_s = 1100$ °C, as shown in Fig. S10.

As demonstrated by Fig. 4(a), herein, we can conclude that SSS and MSS are suitable for preparing As-containing and P-containing MAX phases, respectively. The molten salt [29,42–44] provides a special chemical environment featuring the space confinement effect, faster mass transfer, and strong polarization force contributed by the ionic salts. At high temperatures, the molten salt acts as the solvent for reactants and provides a pool of ionized cations and anions. The solubility and the interactions between the ionized salt and binary/ternary arsenide and phosphorite are different, which should be responsible for the difference between the yield of As/P-containing MAX phases using MSS.

3.4. Physical properties of 321 phases

MAX phases are famous for their outstanding electrical and thermal performances [1,4] among ceramic materials. Meanwhile, some of them are reported to be superconductors [19,45–50]. Here, various characterizations of the intrinsic physical properties at both high and low temperatures were applied by using the as-prepared pure phases of Nb₃P₂C and Nb₃As₂C.

As shown in Fig. 5(a), at high temperatures ($T > 50$ K), the resistivity of Nb₃As₂C (0.3–800 K) and Nb₃P₂C (2–380 K) shows a positively linear temperature dependence, which is commonly

seen in metallic materials. At room temperature, the resistivity of Nb₃As₂C and Nb₃P₂C is $0.53 \mu\Omega \text{ m}$ and $1.34 \mu\Omega \text{ m}$, respectively. The conductivity of Nb₃As₂C is comparable with metal titanium and other MAX phases [4]. The lowest measured temperature is 0.3 K, and no signal of intrinsic superconductivity was observed. Only a resistivity drop around 10 K was detected, which should be attributed to the slight inevitable impurity of NbC with a superconducting temperature around 10 K [51]. The temperature coefficient of resistivity (TCR) is determined by a linear fit of the ρ - T curve at high temperatures, using the equation as follows.

$$\alpha_{\text{TCR}} = \frac{d\rho}{dT \cdot \rho_{300\text{K}}}$$

The residual resistance ratio ($\text{RRR} = R_{300\text{K}}/R_{10\text{K}}$) of Nb₃As₂C is about 4.48 with a TCR $\alpha_{\text{TCR}} = 3.46(1) \times 10^{-3} \text{ K}^{-1}$. For Nb₃P₂C, the RRR and α_{TCR} are smaller than those in Nb₃As₂C, equal to 2.44 and $2.38(1) \times 10^{-3} \text{ K}^{-1}$, respectively.

The Hall coefficient (R_H) was determined by a linear fit of the field-dependent Hall resistance R_{xy} - H curve. As shown in Fig. S11, $R_H = dR_{xy}/dH$, is negative in the measured temperature range suggesting the main carriers are electrons. Here, the single-band model was used, in which $R_H = -1/n_e e$, to determine the carrier concentration (n_e). n_e is in the range of $(1.5\text{--}4.5) \times 10^{22} \text{ cm}^{-3}$, as shown in Fig. 5(b), in which $n = 1.67 \times 10^{22} \text{ cm}^{-3}$ at 300 K. The carrier mobility shows a similar temperature dependence. The mobility is $8.83 \text{ cm}^2 \text{ V}^{-1} \text{ s}^{-1}$ at 300 K, and the max value is $19.05 \text{ cm}^2 \text{ V}^{-1} \text{ s}^{-1}$ at 10 K.

Meanwhile, the MR of Nb₃As₂C (Fig. S13) shows a linear dependence on the magnetic field, as opposed to the typical parabolic behavior in MAX phases [4]. As shown in Fig. 5(c), the MR curve at 10 K can be well fitted linearly, even though the MR is only $\sim 0.1\%$ at 9 T. The linear MR behavior should be attributed to the open orbits of the Fermi surface and the averaging over orientations of the crystallites in polycrystalline samples [52], which will be discussed in the following part.

First-principles calculations were performed to reveal the electronic structure of 321 phases. As shown in Fig. 6(a), The electronic structure shows good metallic behavior, consistent with resistivity measurements. The partial density of states (PDOS) in Fig. 6(b) demonstrates that the states near the Fermi surface are mainly contributed by the d -orbital electrons of the Nb atom. And the Fermi surface (Fig. 6(c)) of Nb₃As₂C shows prominent quasi-two-dimensional characteristics. In the k_x - k_y plane, the Fermi surface is mainly composed of three electron pockets at Γ and one hole pocket at L point. Moreover, some of them show open orbits behavior along the k_z direction, which are responsible for the observed linear MR. The electronic structures of Nb₃P₂C are similar, as shown in Fig. S12.

The thermoelectric properties of Nb₃As₂C are systematically studied, as shown in Fig. 7. A weak Seebeck effect was detected in the measured temperatures. The Seebeck coefficient S is negative in the whole temperature range and its absolute value increases with the increase in temperature. The negative value of S indicates that the main carriers are electrons, which matches the Hall effect results. With the temperature increasing, the Seebeck coefficient is enhanced from $-5.2 \mu\text{V/K}$ at $T = 273$ K to around $-8 \mu\text{V/K}$ at $T = 700$ K. The power factor, $\text{PF} = S^2\sigma$, is also given in Fig. 7(a), where $\sigma = 1/\rho$, ρ is the resistivity, which has been given in Fig. 5(a).

Total thermal conductivity, $\kappa_{\text{tot}} = \kappa_e + \kappa_{\text{lat}}$, in which κ_e and κ_{lat} are the electronic and lattice contribution of thermal conductivity, respectively. κ_e is estimated based on the Wiedemann–Franz law, $\kappa_e = L\sigma T$, where σ is electrical conductivity, T is the absolute temperature, L is the Lorentz number equal to $2.44 \times 10^{-8} \text{ W K}^{-2}$ according to the degenerate limit [54]. By subtracting the electronic contribution, the lattice contribution can be obtained. As

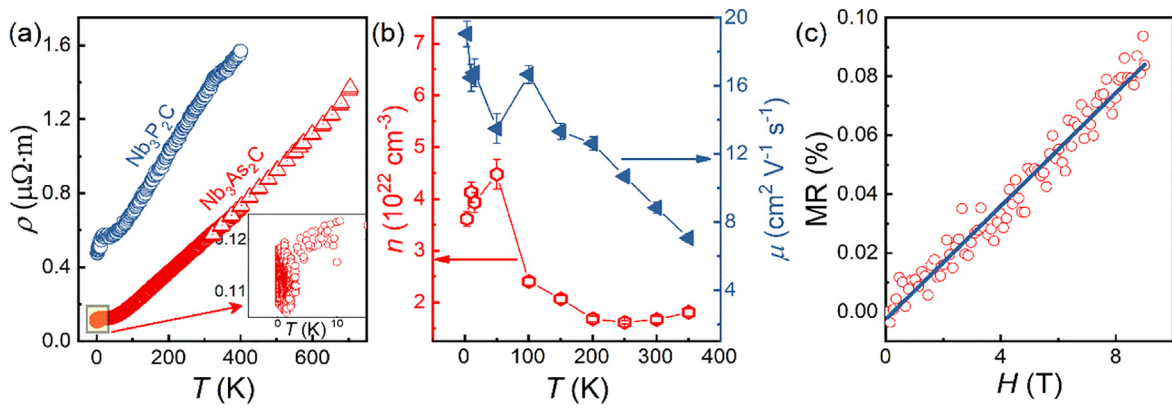


Fig. 5. Magneto-transport properties of Nb₃As₂C and Nb₃P₂C. (a) Temperature-dependent resistivity of Nb₃As₂C (0.3–700 K) and Nb₃P₂C (2–380 K). (b) Temperature-dependent carrier concentration and mobility of Nb₃As₂C. (c) Field-dependent magnetoresistance of Nb₃As₂C at 10 K, the navy line is the linear fit results.

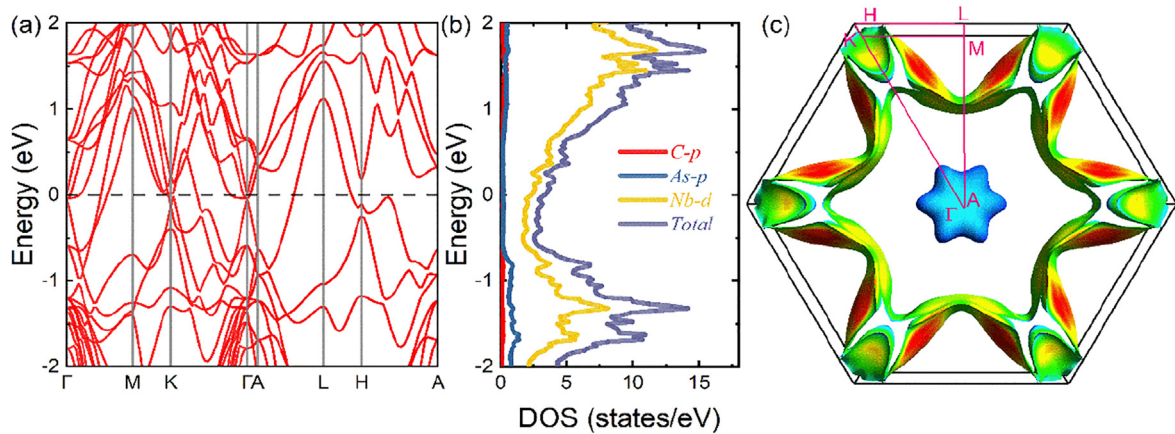


Fig. 6. Electronic structure of Nb₃As₂C. (a) Band structures. (b) Partial density of states. (c) Fermi surface. The Fermi surface was visualized by the FermiSurfer package [53].

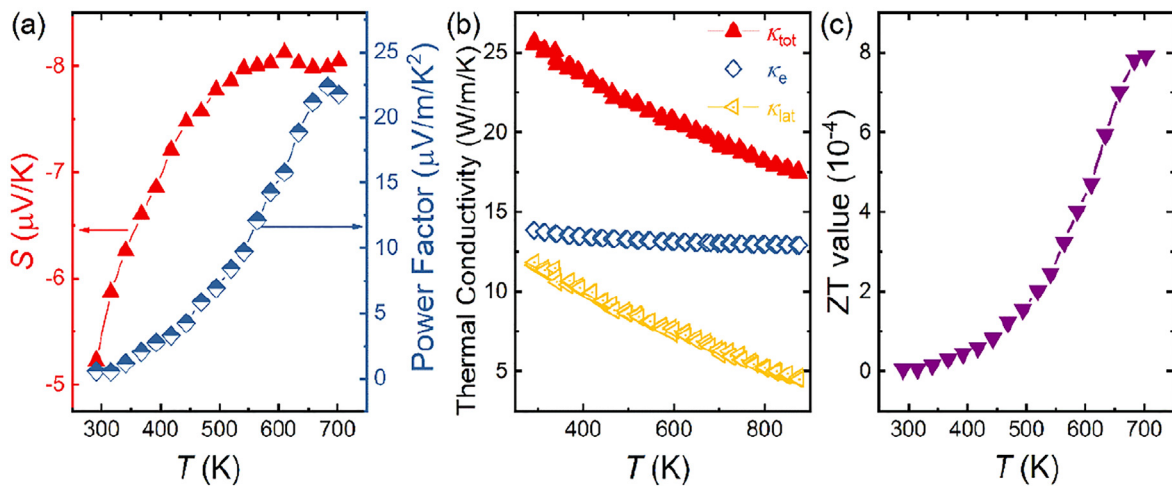


Fig. 7. Thermoelectric properties of Nb₃As₂C. (a) Temperature-dependent Seebeck coefficient and power factor. (b) Temperature dependence of total thermal conductivity (κ_{tot}), and the electronic contribution (κ_e) and lattice contribution (κ_{lat}) of it. (c) Temperature-dependent figure of merit, ZT.

shown in Fig. 7(b), the measured κ_{tot} decreases with the temperature decreases, from 25.7 W m⁻¹ K⁻¹ at 292 K to 17.4 W m⁻¹ K⁻¹ at 876 K. It should be noted that the thermal conductivity may be underestimated due to the density is only around 90%. The value of κ_e (12.92–13.86 W m⁻¹ K⁻¹) does not change significantly with temperature change. While κ_{lat} decreases a lot with temperature decreases, from 11.86 W m⁻¹ K⁻¹ to 4.52 W m⁻¹ K⁻¹. Correspondingly, the value of $\kappa_{\text{lat}} / \kappa_{\text{tot}}$ declines from

46% to 26%, suggesting the decrease of the proportion of electronic contribution in total thermal conductivity with increasing temperature.

The dimensionless figure of merit, $ZT = S^2\sigma T/\kappa_{\text{tot}}$, as a function of temperature is shown in Fig. 7(c). At room temperature, the ZT value is almost negligible, only 6.5×10^{-6} . As previously discussed, S , σ , and $1/\kappa_{\text{tot}}$ all show a positive dependence on temperature. Consequently, the ZT value will increase to 7.9×10^{-4} at 700 K.

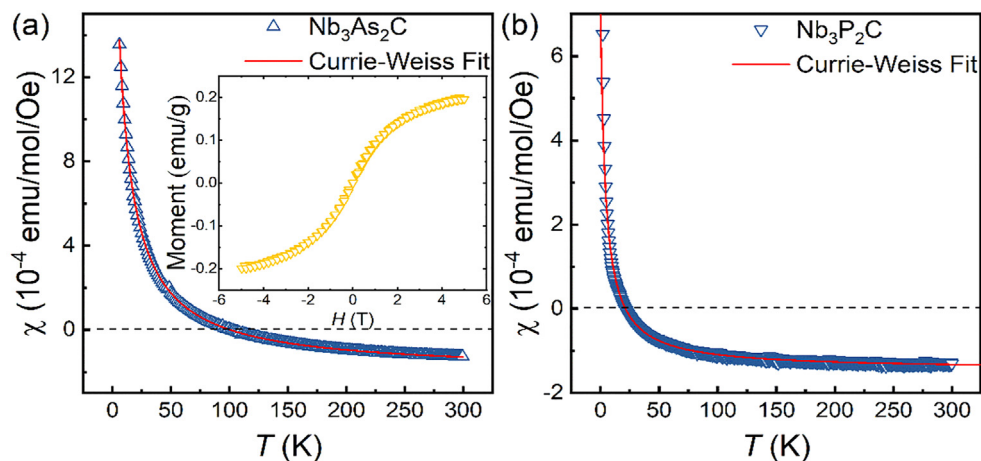


Fig. 8. Magnetic properties of (a) $\text{Nb}_3\text{As}_2\text{C}$ and (b) $\text{Nb}_3\text{P}_2\text{C}$. The inset of (a) is the $M-H$ curve at 10 K.

As shown by the temperature-dependent magnetic susceptibility ($\chi-T$) in Fig. 8, both paramagnetic and diamagnetic signals are detected in the $\text{Nb}_3\text{As}_2\text{C}$ and $\text{Nb}_3\text{P}_2\text{C}$. As shown in Fig. 8, the temperature-dependent susceptibility can be well fitted by the Currie-Weiss law $\chi = \chi_0 + C/(T - \theta_{\text{CW}})$, where C is the Currie-Weiss constant, θ_{CW} is the Currie-Weiss temperature, and χ_0 is a constant contributed by the diamagnetism. According to the Currie-Weiss fitting results, θ_{CW} of $\text{Nb}_3\text{As}_2\text{C}$ and $\text{Nb}_3\text{P}_2\text{C}$ is close to zero, equal to $-2.01(4)$ K and $-4.75(4)$ K, respectively. Meanwhile, no obvious hysteresis was observed in the field-dependent magnetization measured at 10 K, as shown in the inset of Fig. 8(a), supporting the Currie-Weiss paramagnetism in $\text{Nb}_3\text{As}_2\text{C}$. The diamagnetic contribution to the magnetism of $\text{Nb}_3\text{P}_2\text{C}$ is stronger than the one in $\text{Nb}_3\text{As}_2\text{C}$, in which the susceptibility is negative when $T > 21$ K, while the critical temperature of $\text{Nb}_3\text{As}_2\text{C}$ is around 101 K.

4. Conclusions

In conclusion, the process and mechanism to synthesize $\text{Nb}_3\text{P}_2\text{C}$ and other As/P-containing MAX phases and the intrinsic physical properties of 321 phases, were systematically studied here. We demonstrated that synthesis method, reaction route, and sintering temperature are the three crucial factors to obtain their high-purity phases. Using MSS, an almost pure phase (99%) of $\text{Nb}_3\text{P}_2\text{C}$ can be obtained, which is significantly enhanced in contrast to the limited purity ($< 66\%$) by SSS. Based on the experimental results and first-principles calculations, the chemical reaction route $\text{NbP} + \text{Nb} + \text{C} \rightarrow \text{Nb}_3\text{P}_2\text{C}$ is most applicable for the phase formation of $\text{Nb}_3\text{P}_2\text{C}$. And the advantage of the MSS method is the facilitation of three possible reaction routes, especially on $\text{Nb}_2\text{PC} + \text{NbP} \rightarrow \text{Nb}_3\text{P}_2\text{C}$. Meanwhile, the feasibility of SSS and MSS to synthesize other As/P-containing MAX phases, including $\text{Nb}_3\text{As}_2\text{C}$, Nb_2PC , and Nb_2AsC , were carefully checked. We found that MSS is also effective in synthesizing Nb_2PC , in which the purity can be greatly improved to $> 75\%$ in contrast to $< 30\%$ by SSS. However, MSS is not applicable to As-containing MAX phases, which can be prepared in the pure phase by SSS. By characterizing the intrinsic physical properties of pure $\text{Nb}_3\text{P}_2\text{C}$ and $\text{Nb}_3\text{As}_2\text{C}$, with the help of first-principles calculations, electron-type carriers, negative Seebeck coefficient, and linear MR were detected, which could be well explained by the electron-orbits and open-orbits in Fermi surface. Meanwhile, well electrical and thermal conductivity, weak thermoelectric effect, and coexistence of Currie-Weiss paramagnetism and diamagnetism were demonstrated. Our work provides a guide to synthesizing As/P-containing MAX phases, and the

intrinsic physical properties of $\text{Nb}_3\text{P}_2\text{C}$ and $\text{Nb}_3\text{As}_2\text{C}$ given here are helpful to explore the future potential applications of 321 phases.

Author contributions

H.X. Chen and P.Q. Dai conceived this project. H.X. Chen, S. Li, and Z.L. Zhang performed the sample synthesis. H.X. Chen and S. Li, performed the physical property characterizations. H.X. Chen, J. Deng, and S.X. Du analyzed the physical properties. J. Deng, and S.X. Sun performed the first-principles calculations. S. Li and L. Huang performed the TEM characterizations. J.N. Huang and F. Chang characterized and analyzed the micro-morphology. H.X. Chen, J. Deng, S.X. Du, and P.Q. Dai wrote the manuscript with the contribution of all the authors.

Declaration of Competing Interests

The authors declare that they have no known competing financial interests or personal relationships that could have appeared to influence the work reported in this paper.

Acknowledgments

This work was financially supported by the National Science Foundation for Young Scientists of China (No. 51902055) and the Natural Science Foundation of Fujian Province (Nos. 2021J011077, 2021J05224, and 2020J01898).

Supplementary materials

Supplementary material associated with this article can be found, in the online version, at doi:10.1016/j.jmst.2022.06.016.

References

- [1] M.W. Barsoum, *Prog. Solid State Chem.* 28 (2000) 201–281.
- [2] H.X. Chen, D.L. Yang, Q.H. Zhang, S.F. Jin, L.W. Guo, J. Deng, X.D. Li, X.L. Chen, *Angew. Chem-Int. Ed.* 58 (2019) 4576–4580.
- [3] P. Eklund, M. Beckers, U. Jansson, H. Högborg, L. Hultman, *Thin Solid Films* 518 (2010) 1851–1878.
- [4] M.W. Barsoum, *MAX Phases, Properties of Machinable Ternary Carbides and Nitrides*, Wiley-VCH Verlag GmbH & Co. KGaA, Weinheim, Germany, 2013.
- [5] M. Li, Y.B. Li, K. Luo, J. Lu, P. Eklund, P. Persson, J. Rosen, L. Hultman, S.Y. Du, Z.R. Huang, Q. Huang, *J. Inorg. Mater.* 34 (2019) 60–64.
- [6] V. Kamysbayev, A.S. Filatov, H. Hu, X. Rui, F. Lagunas, D. Wang, R.F. Klie, D.V. Talapin, *Science* 369 (2020) 979–983.
- [7] M. Naguib, M.W. Barsoum, Y. Gogotsi, *Adv. Mater.* 33 (2021) 2103393.
- [8] A. VahidMohammadi, J. Rosen, Y. Gogotsi, *Science* 372 (2021) eabf1581.
- [9] Z.G. Du, C. Wu, Y.C. Chen, Z.J. Cao, R.M. Hu, Y.Z. Zhang, J.N. Gu, Y. Cui, H. Chen, Y.Z. Shi, J.X. Shang, B. Li, S.B. Yang, *Adv. Mater.* 33 (2021) 2101473.

- [10] S.K. Nemani, B. Zhang, B.C. Wyatt, Z.D. Hood, S. Manna, R. Khaledialidusti, W. Hong, M.G. Sternberg, S.K.R.S. Sankaranarayanan, B. Anasori, *ACS Nano* 15 (2021) 12815–12825.
- [11] M. Sokol, V. Natu, S. Kota, M.W. Barsoum, *Trends Chem.* 1 (2019) 210–223.
- [12] L.F. He, Y.W. Bao, J.Y. Wang, M.S. Li, Y.C. Zhou, *Acta Mater.* 57 (2009) 2765–2774.
- [13] L.Y. Zheng, J.M. Wang, X.P. Lu, F.Z. Li, J.Y. Wang, Y.C. Zhou, *J. Am. Ceram. Soc.* 93 (2010) 3068–3071.
- [14] J.Y. Wang, Y.C. Zhou, *Annu. Rev. Mater. Res.* 39 (2009) 415–443.
- [15] M.A. Hadi, M.A. Rayhan, S.H. Naqib, A. Chroneos, A.K.M.A. Islam, *Comput. Mater. Sci.* 170 (2019) 109144.
- [16] R.S. Kumar, S. Rekhi, A.L. Cornelius, M.W. Barsoum, *Appl. Phys. Lett.* 86 (2005) 111904.
- [17] M.A. Hadi, S.R.G. Christopoulos, A. Chroneos, S.H. Naqib, A.K.M.A. Islam, *Mater. Today Commun.* 25 (2020) 101499.
- [18] T.H. Scabarozzi, S. Amini, O. Leaffer, A. Ganguly, S. Gupta, W. Tambussi, S. Clipper, J.E. Spanier, M.W. Barsoum, J.D. Hettinger, S.E. Lofland, *J. Appl. Phys.* 105 (2009) 013543.
- [19] S.E. Lofland, J.D. Hettinger, T. Meehan, A. Bryan, P. Finkel, S. Gupta, M.W. Barsoum, G. Hug, *Phys. Rev. B* 74 (2006) 174501.
- [20] T. Liao, J. Wang, Y. Zhou, *J. Phys. Condens. Matter* 18 (2006) 6183–6192.
- [21] A. Dash, R. Vaßen, O. Guillon, J. Gonzalez-Julian, *Nat. Mater.* 18 (2019) 465–470.
- [22] H. Fashandi, M. Dahlqvist, J. Lu, J. Palisaitis, S.I. Simak, I.A. Abrikosov, J. Rosen, L. Hultman, M. Andersson, A. Lloyd Spetz, P. Eklund, *Nat. Mater.* 16 (2017) 814–818.
- [23] Y.B. Li, H. Shao, Z.F. Lin, J. Lu, L.Y. Liu, B. Duployer, P.O.Å. Persson, P. Eklund, L. Hultman, M. Li, K. Chen, X.H. Zha, S.Y. Du, P. Rozier, Z.F. Chai, E. Raymundo-Piñero, P.L. Taberna, P. Simon, Q. Huang, *Nat. Mater.* 19 (2020) 894–899.
- [24] T. Galvin, N.C. Hyatt, W.M. Rainforth, I.M. Reaney, D. Shepherd, *J. Eur. Ceram. Soc.* 38 (2018) 4585–4589.
- [25] A.M. Abdelkader, *J. Eur. Ceram. Soc.* 36 (2016) 33–42.
- [26] Y. Zhong, Y. Liu, J.W. Ye, N. Jin, Z.F. Lin, *J. Am. Ceram. Soc.* 105 (2022) 2277–2287.
- [27] M. Li, J. Lu, K. Luo, Y.B. Li, K.K. Chang, K. Chen, J. Zhou, J. Rosen, L. Hultman, P. Eklund, P.O.Å. Persson, S.Y. Du, Z.F. Chai, Z.R. Huang, Q. Huang, *J. Am. Chem. Soc.* 141 (2019) 4730–4737.
- [28] Y.G. Gogotsi, R.A. Andrievski, *Materials Science of Carbides, Nitrides and Borides*, Springer, Netherlands, Dordrecht, 1999.
- [29] T. Kimura, in: C. Sikalidis, *Advances in Ceramics – Synthesis and Characterization, Processing and Specific Applications*, IntechOpen, London, 2011.
- [30] J. Rodríguez-Carvajal, *Physica B* 192 (1993) 55–69.
- [31] N.V.Y. Scarlett, I.C. Madsen, *Powder Diffr.* 21 (2006) 278–284.
- [32] C. Giannini, A. Guagliardi, R. Millini, *J. Appl. Crystallogr.* 35 (2002) 481–490.
- [33] D.L. Bish, S.A. Howard, *J. Appl. Crystallogr.* 21 (1988) 86–91.
- [34] G. Kresse, J. Furthmüller, *Comput. Mater. Sci.* 6 (1996) 15–50.
- [35] G. Kresse, J. Furthmüller, *Phys. Rev. B* 54 (1996) 11169–11186.
- [36] G. Kresse, D. Joubert, *Phys. Rev. B* 59 (1999) 1758–1775.
- [37] J.P. Perdew, K. Burke, M. Ernzerhof, *Phys. Rev. Lett.* 78 (1997) 1396.
- [38] H.J. Monkhorst, J.D. Pack, *Phys. Rev. B* 13 (1976) 5188–5192.
- [39] A. Togo, I. Tanaka, *Scr. Mater.* 108 (2015) 1–5.
- [40] Z.H. Tian, F.S. Wu, P.Y. Hu, J.X. Ding, Y. Zhang, P.G. Zhang, Z.M. Sun, *J. Alloy. Compd.* 894 (2022) 162429.
- [41] O. Beckmann, H. Boller, H. Nowotny, *Mon. Chem.* 99 (1968) 1580–1583.
- [42] X. Liu, N. Fechner, M. Antonietti, *Chem. Soc. Rev.* 42 (2013) 8237–8265.
- [43] S.V. Volkov, *Sov. Prog. Chem.* 55 (1989) 1–8.
- [44] M. Xiao, B. Luo, M. Konarova, Z.L. Wang, L.Z. Wang, *Eur. J. Inorg. Chem.* 2020 (2020) 2942–2949.
- [45] P. Eklund, J. Rosen, P.O.Å. Persson, *J. Phys. D-Appl. Phys.* 50 (2017) 113001.
- [46] K. Sakamaki, H. Wada, H. Nozaki, Y. Onuki, M. Kawai, *Solid State Commun.* 112 (1999) 323–327.
- [47] A.D. Bortolozzo, O.H. Sant’Anna, C.A.M. dos Santos, A.J.S. Machado, *Solid State Commun.* 144 (2007) 419–421.
- [48] R. Meshkian, A.S. Ingason, M. Dahlqvist, A. Petruhins, U.B. Arnalds, F. Magnus, J. Lu, J. Rosen, *Phys. Status Solidi-Rapid Res. Lett.* 9 (2015) 197–201.
- [49] L.E. Toth, *J. Less Common Met.* 13 (1967) 129–131.
- [50] A.D. Bortolozzo, Z. Fisk, O.H. Sant’Anna, C.A.M. dos Santos, A.J.S. Machado, *Physica C* 469 (2009) 256–258.
- [51] R.H. Willens, E. Buehler, B.T. Matthias, *Phys. Rev.* 159 (1967) 327–330.
- [52] I. Lifshitz, V. Peschanskii, *Sov. Phys. JETP* 8 (1959) 875–883.
- [53] M. Kawamura, *Comput. Phys. Commun.* 239 (2019) 197–203.
- [54] Charles Kittel, *Introduction to Solid State Physics*, 8th ed., John Wiley & Sons, Inc, New York, 2004.